Chemical Engineering Journal 523 (2025) 167169

Contents lists available at ScienceDirect

Chemical Engineering Journal

journal homepage: www.elsevier.com/locate/cej

Ni-Co-O anodes for the alkaline oxygen evolution reaction: Multistage electrode optimization and plasma-assisted activity enhancement enabled by a coherent workflow☆

Vineetha Vinayakumar [a,b,*], Timo Wagner [c], Christian Marcks [d], Jacob Johny [e], Garlef Wartner [e,f], Ahyoun Lim [e], Marc F. Tesch [e], Ioannis Spanos [e], Aliakbar Ghafari [e,f], Adarsh Jain [a], Oleg Prymak [g], Ignacio Sanjuán [b,h], Ahammed Suhail Odungat [a], Osama Anwar [a], Mohit Chatwani [a], Aneeta Jose [a], Vimanshu Chanda [h], Axel Knop-Gericke [e,f], Corina Andronescu [b,h], Anna K. Mechler [d], Nicolas Wöhrl [b,c], Doris Segets [a,b,*]

[a] Institute for Energy and Materials Processes – Particle Science and Technology (EMPI-PST), University of Duisburg-Essen, Carl-Benz-Straße 199, 47057 Duisburg, Germany
[b] Center for Nanointegration Duisburg-Essen (CENIDE), University of Duisburg-Essen, Carl-Benz-Straße 199, 47057 Duisburg, Germany
[c] Faculty of Physics, University of Duisburg–Essen (UDE), Duisburg, Germany
[d] Electrochemical Reaction Engineering, RWTH Aachen University, Forckenbeckstraße 51, 52074 Aachen, Germany
[e] Max Planck Institute for Chemical Energy Conversion, Stiftstr. 34-36, 45470 Mülheim an der Ruhr, Germany
[f] Fritz-Haber-Institute of the Max-Planck-Society, Department of Inorganic Chemistry, Faradayweg 4-6, 14195 Berlin, Germany
[g] Institute for Inorganic Chemistry and Center for NanoIntegration (CENIDE), University of Duisburg-Essen, Universitätsstr. 5–7, 45117 Essen, Germany
[h] Chemical Technology III, University of Duisburg-Essen, Carl-Benz-Str. 199, 47057 Duisburg, Germany

ARTICLE INFO

Keywords:
Alkaline water electrolysis
Plasma processing
Ultrasonic spray coating
Operando analysis
Ink formulation
In-line processing

ABSTRACT

Improving the performance of oxygen evolution reaction (OER) catalysts through proper catalyst design and processing represents a critical step toward enhancing the efficiency of water electrolysis. While many studies focus on structure-activity relationships and mechanistic insights confined to a particular stage during the anode fabrication, an integrated approach covering all process steps is crucial to optimize performance-relevant properties such as composition, morphology, and electrode architecture. In this study, we demonstrate a comprehensive approach for developing Ni-Co-O anodes as a model system through the entire process chain. Starting from the initial powder characterization through *operando* to post-catalysis analyses, we first underpin the critical impact of catalyst ink optimization through solvent matrix screening, enabling high-quality electrode layers via ultrasonic spray coating on Ni plates. This enables us to uncover the effects of post nitrogen plasma treatment integrated into our coherent workflow yielding binder-free Ni-Co-O anode surfaces with enhanced redox reversibility, Fe uptake, porosity, and wettability. These improvements reduce the OER overpotential by ~43 mV at 100 mA/cm^2 compared to untreated counterparts. The durable performance of these electrodes is further demonstrated in a single cell configuration. Our holistic approach from catalyst powder to post-mortem analysis highlights the benefits of a coherent anode development strategy employing plasma post-processing which is broadly applicable and easily transferable to other benchmark electrocatalysts.

1. Introduction

The urgent need to develop renewable and clean energy solutions, driven by the depletion of fossil fuels and the imperative to combat global warming, has propelled hydrogen as a promising alternative for energy storage characterized by zero pollution, high specific energy density, and abundant sources [1–3]. Electrochemical water splitting, evolving over two centuries since its discovery in the 18th century, is

☆ This article is part of a Special issue entitled: 'Electrochemical Energy' published in Chemical Engineering Journal.

* Corresponding authors at: Institute for Energy and Materials Processes – Particle Science and Technology (EMPI-PST), University of Duisburg-Essen, Carl-Benz-Straße 199, 47057 Duisburg, Germany.
E-mail addresses: vineetha.vinayakumar@uni-due.de (V. Vinayakumar), doris.segets@uni-due.de (D. Segets).

https://doi.org/10.1016/j.cej.2025.167169
Received 18 May 2025; Received in revised form 3 August 2025; Accepted 11 August 2025
Available online 12 August 2025

becoming pivotal for large-scale hydrogen production [4]. Despite its potential, challenges like production cost and efficiency directly influence its advancement [5]. Even though significant progress in industrial alkaline and acidic water electrolysis has been achieved, the OER at the anode still remains a critical bottleneck due to the sluggish kinetics [6,7]. Catalysts play a vital role in enhancing OER efficiency by reducing overpotential and improving electrocatalytic performance [8,9]. Current research efforts are thus concentrated on developing highly active OER electrocatalysts to advance further in the overall efficiency and materials-stability during electrocatalytic water splitting [10,11]. The ideal OER electrocatalyst should possess high intrinsic activity and demonstrate long-term electrochemical stability to withstand harsh reaction environments [12]. Since electrocatalysts play a pivotal role in determining the overall performance of electrochemical systems, comprehensive characterization of the electrodes, along with the implementation of suitable post-processing strategies, is essential for the development of high-performance OER catalysts.

The current benchmark OER electrocatalysts are based on precious metals (e.g., Ir and Ru) and their oxides (e.g., IrO_2 and RuO_2) typically in acidic electrolytes [13–16]. However, their low abundance, high cost, and poor chemical stability in alkaline media pose a challenge to their tenable application and hence demand the use of catalysts based on more earth-abundant and economic elements [17–19]. Hence, significant efforts have been directed toward developing efficient alkaline OER catalysts using non-precious transition metals [20,21]. Examples include materials based on nickel (Ni), cobalt (Co), iron (Fe), and manganese (Mn) which have garnered substantial interest from researchers due to their tunable physicochemical properties and electronic structures that could be used to tune the resulting electrochemical activity [22–26]. In particular, combinations of different metals from this library such as Ni and Co are favored for their adjustable chemical reactivity, theoretical efficiency, and stability under alkaline conditions [27–29]. Ni-Co-based electrocatalysts also possess suitable atomic and electronic structures exposing more active sites and atomic defects, which show high activity, stability, and corrosion resistance during the OER process [25,30].

Next to the intrinsic properties of the catalyst, the characteristics of the final anode (the electrode at which OER occurs) are equally important for defining the electrochemical activity and stability in a setting relevant for technical application. This includes features such as the morphology and particle size, adhesion properties, wetting, and surface roughness of the final electrode, which can all impact its final performance. To date, several physical, chemical, and colloidal deposition techniques are used to obtain anodes [31]. One promising method among these is ultrasonic spray coating, which involves the spray deposition of an ink containing the desired material onto a suitable support, thus achieving a compact active layer [32]. In case of the electrode fabrication by ultrasonic spray coating, the process involves multiple stages starting from the powder material preparation followed by the formulation of a stable catalyst ink and final spray deposition to obtain solid electrodes. This demands characterization and continuous optimization throughout the entire process chain rather than focusing on only one stage during the anode development. Optimization of the electrode in each stage is crucial as this affects the following stage and defines the extrinsic properties of the final anodes and their performance [33]. However, comprehensive studies encompassing full system characterization and optimization within a coherent workflow remain rare, particularly for critically important material systems such as Ni-Co-based anodes for alkaline water electrolysis (AWE). Most existing approaches focus on isolated aspects of catalyst development, either powder synthesis, ink formulation, or post-processing, without establishing a systematic understanding of how processing parameters at each stage influence the final electrode performance. Furthermore, while plasma post-processing has shown promise for catalyst enhancement, the underlying mechanisms responsible for performance improvements remain poorly understood, particularly regarding the interplay between plasma-induced structural changes, surface chemistry modifications, and electrochemical activity.

Herein, we present a coherent workflow for Nickel-Cobalt-Oxide (Ni-Co-O) as a model system for alkaline OER through the entire anode development chain. Our investigations start with a thorough characterization of the commercial Ni-Co-O powder, followed by the development and formulation of a stable catalyst ink, and final fabrication of electrodes on Ni plates through ultrasonic spray coating. In each step, we utilized a set of tools to identify and optimize crucial properties that influence the final application of these electrodes. We show that post treatment of the anodes by a nitrogen plasma integrated in our coherent workflow yields binder-free electrodes with enhanced surface properties contributing to an overall enhancement in the activity. The novelty of our work lies in three key aspects: (i) We provide the first comprehensive characterization approach that systematically tracks catalyst properties from the initial powder state through ink formulation to final coated layers, enabling insight into process-structure-performance relationships. (ii) We demonstrate a novel insulator-confined plasma post-processing strategy that achieves controlled heterostructure formation and intentional binder removal, leading to significant performance enhancement in both AWE and anion exchange membrane water electrolysis (AEMWE) configurations. (iii) We establish clear mechanistic understanding of plasma-induced modifications through advanced *operando* and *ex situ* characterization techniques, revealing how plasma treatment simultaneously modifies morphology, surface chemistry, and electronic structure to enhance OER activity. By closing the loop from powder studies to layer property assessment before and after plasma-post-processing, electrochemical characterization including single cell measurements, *operando,* and post-mortem studies, the developed coherent workflow enables a continuous and knowledge-based electrode advancement within the available wide parameter space.

2. Results and discussion

2.1. Characterization of the Ni-Co-O powder

2.1.1. Particle size, structure, and composition analysis

The Ni-Co-O commercial powder was first thoroughly characterized by a set of complementary analytical techniques. A detailed discussion on powder characterization can be found in the supplementary information. In short, transmission electron microscopy with energy dispersive X-Ray spectroscopy (TEM-EDX) showed a cube-like shape with largely varying primary particle sizes in the range 10–150 nm with a mean particle size (diagonally measured on more than 200 particles) of 54 ± 41 nm (inset) with homogeneous distribution of Ni, Co, and O (**Fig. S1 and S2**). X-ray diffraction (XRD), Raman and X-ray photoelectron measurements (**Fig. S3**) confirmed the structural and phase integrity of the commercial powder and validated the Ni-Co-O phase in agreement with the TEM-EDX analysis.

2.1.2. Dispersibility by Hansen solubility parameters (HSP)

Understanding the intricate relationship between probe liquids and catalyst materials in a colloidal dispersion is crucial since liquids are used to transport catalyst materials throughout the coating and drying process. Hence, after thoroughly characterizing the Ni-Co-O powder in the dry state, we analyzed the powder-liquid interaction with probe liquids of known polarity to assess the particles' surface properties and to rationally select the composition of the continuous phase for the ink formulation.

According to HSP theory, the three parameters from dispersion forces (δ_D), dipolar intermolecular force (δ_P), and hydrogen bonds (δ_H) between probe liquids and catalyst particles can be represented as coordinates in the three-dimensional Hansen space [34,35]. In line with our previous works [36], we used the two-step procedure of Amin et al. to select the appropriate probe liquids for determining HSP of Ni-Co-O. In the first step, the interaction of the material with the three initial

probe liquids of different protic behavior namely - ethanol (EtOH: protic polar), dimethylformamide (DMF: aprotic polar), tetrahydrofuran (THF: moderate polar) is observed. Based on which probe liquids in the first step formed sedimentation-stable dispersions or not, further probe liquids were added accordingly to define the probe liquid list for determining HSP. In case of Ni-Co-O, in the first step, all three initial probe liquids namely EtOH, DMF, and THF, enabled stable dispersions with Ni-Co-O. This meant that the material interacted well with all protic, aprotic, and polar probe liquids and so. Hence, in the second step, isopropanol (IPA), acetone (Ace), dimethyl sulfoxide (DMSO), 1,4. Dioxane (Diox) and toluene (Tol) were added.

The relative sedimentation times, determined from the evolution of the integral extinction of the sedimenting dispersions, were used to rank these eight probe liquids from the best to the least compatible solvent (details in section 4.1.1). The HSPiP program was used to calculate HSP of the material using the automated-addition-method developed by Süß et al. [37]. Accordingly, the resulting HSP of Ni-Co-O and its HSP sphere are shown in Fig. 1.

This study reveals a higher contribution to hydrogen bonding interactions and dipolar interactions allowing the catalyst powder to disperse readily in most of the chosen probe liquids. Here, it should be noted that water was not considered within the given HSP sphere due to its high hydrogen bonding capabilities ($\delta_H = 42$ MPa$^{1/2}$), making a large distance compared to other chosen solvents [38] and leading to errors in HSP determination. However, due to cost considerations and since water is one of the commonly used liquids in generating stable catalyst inks, we included water in the final ink formulations [39]. The determined HSP serve to characterize the material and provide insights into its surface behavior. This can assist in comparison between similar materials in addition to selection of the appropriate probe liquids for ink formulation.

2.1.3. Ni-Co-O ink formulation

The sedimentation behavior of catalyst nanopowders in different solvent systems is shown in Fig. 2, which reflects the dispersions actually used for ink formulation in this study. Transmittograms [40,41] were applied to analyze dispersions prepared in both pure water and a water-EtOH mixture with Nafion binder. These transmittograms, which are contour plots illustrating time and space-resolved transmission, were generated from centrifugation data to offer insights into sedimentation dynamics and colloidal stability.

In each transmittogram, the x-axis represents the elapsed time since centrifugation began, and the y-axis shows the radial position within the centrifuge cell. Transmission values are represented by varying gray tones, with darker tones indicating higher levels of light blockage due to scattering, corresponding to higher particle concentration at a given time and position.

Fig. 2 compares sedimentation profiles for the two solvent systems: (a) pure water and (b) a 1:1 water-EtOH mixture, both containing Nafion as the binder. In pure water (Fig. 2a), sedimentation occurs quickly, with high transmission levels appearing early in the process and minimal gradient development, suggesting rapid particle settling. In contrast, the water-EtOH mixture (Fig. 2b) exhibits slower sedimentation with a more gradual transmission gradient over time, indicating a reduced particle settling rate and improved colloidal stability.

Under a relative centrifugal acceleration (RCA) of 733.69, complete sedimentation of particles in the water-based dispersion occurred in approximately 8 min, equivalent to roughly 4 days, and 8 h at gravity (RCA = 1). For the water-EtOH mixture, complete sedimentation took approximately 25 min, translating to around 13 days and 2 h at gravity. The slower sedimentation rate observed upon dispersion in the water-EtOH mixture suggests that this solvent combination improves colloidal stability, potentially making it more suitable for applications requiring prolonged stability and homogeneous anode layers.

2.2. Ni-Co-O layer deposition and plasma post-treatment

Coated Ni-Co-O layers were obtained by spray deposition of the Ni-Co-O ink onto Ni plate substrates (Fig. 3a, for details see section 4.3). Ultrasonic spray coating possesses several advantages in general such as good reproducibility and transfer efficiency, precise conformal coating, and simplicity [42]. After the deposition of the layers on Ni plates, the resulting Ni/Ni-Co-O samples were post-treated under a nitrogen plasma. Plasma treatment was applied due to its capability to alter surface properties, such as morphology, wettability, and chemical composition. It is particularly interesting as it affects the oxide phases which are all crucial in AWE [43,44]. A first indication for a successful modification of the surface is given already by a change in visual appearance, as the plasma-processed electrodes appeared darker compared to the as-prepared Ni-Co-O layers (**Fig. S4**). A comprehensive analysis of the plasma-induced changes in the physicochemical properties of the anode are discussed in detail in the following sections.

2.2.1. Surface topography of the Ni-Co-O layers

To identify the surface of the electrodes before and after plasma treatment, scanning electron microscopy (SEM) analysis was performed

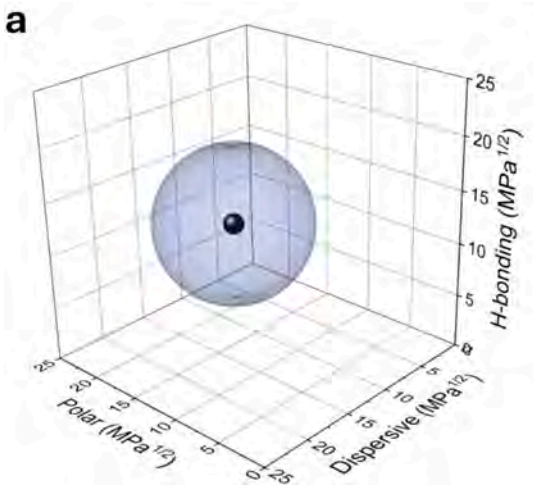

b

Material	Ni-Co-O
Disperse interactions δ_D (MPa$^{1/2}$)	15.2
Polar interactions δ_P (MPa$^{1/2}$)	12.3
Hydrogen bonding δ_H (MPa$^{1/2}$)	13.6
Sphere radius (MPa$^{1/2}$)	6.9
Outliers	0
Fitting	1

Fig. 1. HSP determination of Ni-Co-O with probe liquid selection done by the two-step procedure followed by automated addition to determine the final HSP. The HSP of Ni-Co-O (a) are shown with the HSP sphere outline representing the region of good interaction with solvents, while HSP coordinates are summarized in the table on the right.

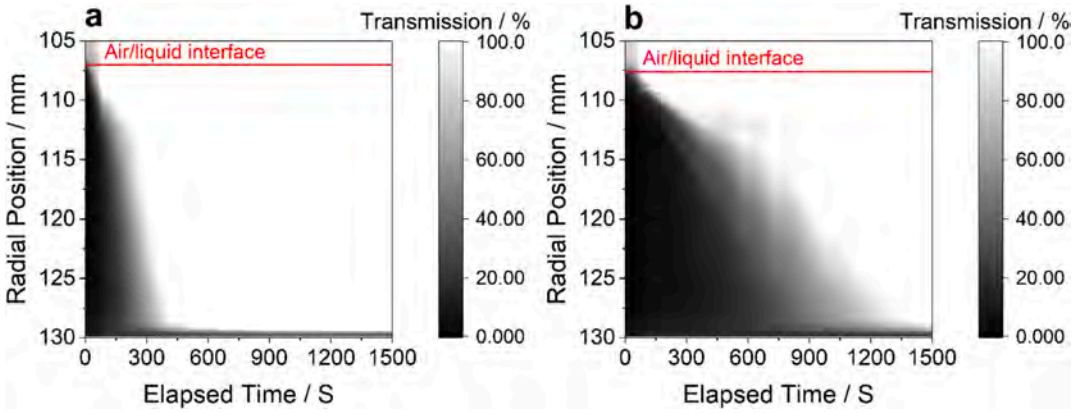

Fig. 2. Visualization of the time-resolved sedimentation process via transmittograms: (a) Ink prepared using pure water as a solvent, and (b) an ink prepared using a mixture of water and EtOH as continuous phase (1:1 volume ratio), both containing Nafion as a binder.

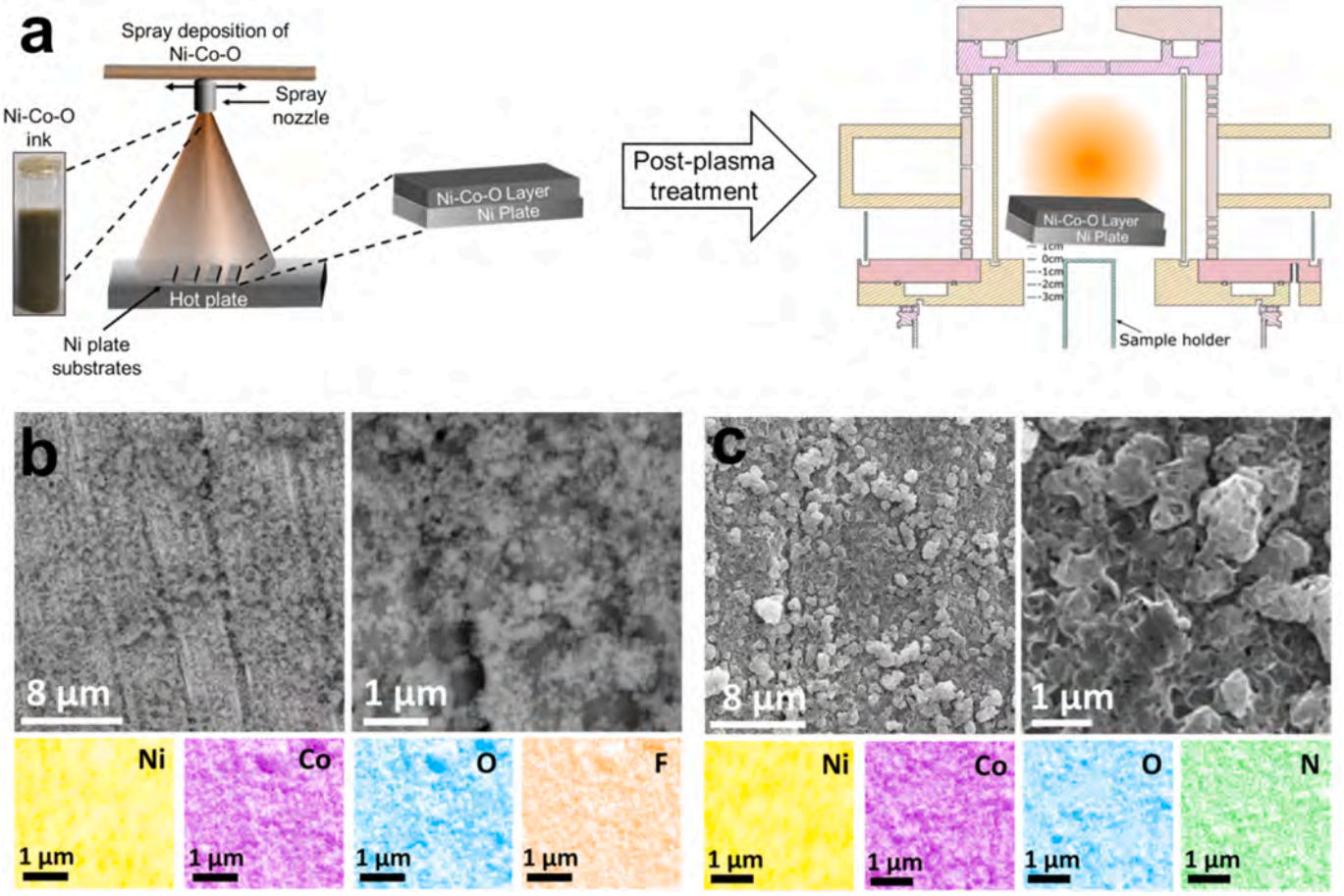

Fig. 3. (a) Schematic representation showing the spray deposition of Ni-Co-O layers on Ni plate substrates and the N_2 plasma post treatment on the coated layers. SEM and EDX analysis conducted on the (b) as-prepared and (c) plasma-treated Ni-Co-O films deposited on Ni plate substrates.

on the coated Ni-Co-O layers. When Kong et al. applied post-treatment by nitrogen plasma onto NiCo-layered double hydroxide (LDH), the surface was distorted and roughened, and they found a higher density of micropores and mesopores which were attributed to the bombardment of the energetic particles and active hydrogen-mediated etching inside the plasma [45]. Fig. 3b and c show the surface morphology of the as-prepared and plasma-treated Ni-Co-O at two different magnifications along with the corresponding EDX mappings. Also in our case, a significant transformation of the surface of the coated layers is noted after the plasma treatment. The more spherical particle-like structures in the as-prepared films turn into a more interconnected flake-like structure with apparent higher porosity after the plasma treatment. In particular, it is often reported that a more porous structure of the catalyst layers is advantageous for electrochemical applications because the electrodes exhibit increased surface area and fast mass diffusion leading to enhanced activity [46,47]. Since the porosity might play a crucial role in their application as electrodes, a more detailed analysis of the pore structure in these spray-deposited Ni-Co-O layers was indispensable. EDX analysis detected Ni, Co, and O in both as-prepared and plasma-treated films as expected, while F was detected in as-prepared layers

due to Nafion and N in plasma-treated Ni-Co-O due to the N_2 plasma (**Fig. S5**).

TEM analysis was subsequently conducted to determine the overall appearance of the Ni-Co-O particles on the as-prepared and plasma-treated Ni-Co-O films and to investigate any changes in the particle size after film deposition and plasma post-treatment (**Fig. S6**). To this end, particles were scratched from the spray-deposited layers on the Ni plate and subsequently analyzed. The as-deposited Ni-Co-O layers showed an average particle size of 57 nm (Fig. S6a) thus matching the average size obtained for the commercial Ni-Co-O powder (54 nm). Interestingly, plasma post-treatment led to a size reduction of the primary Ni-Co-O particles down to ~14 nm that are more irregularly shaped as shown in Fig. S6b. This substantial particle size reduction is attributed to thermally modulated phase restructuring during insulator-confined plasma processing, where localized thermal accumulation enhances the mobility of surface species and enables controlled heterostructure formation, similar to mechanisms reported by Ouyang et al. [48]. The elevated substrate temperature during our plasma treatment significantly enhances reaction kinetics of surface species, enabling partial restructuring while preserving underlying phases and leading to spatially distinct interfaces [49]. The EDX maps conducted on the as-prepared Ni-Co-O samples identified all expected elements (Ni, Co, and O), and in addition C from the Nafion binder used for the catalyst ink preparation (see experimental section for details). In case of the N_2 plasma-treated Ni-Co-O particles, in addition to the homogeneous distribution of Ni, Co, and O, N was also detected.

To evaluate the topography of the anodes in more detail, atomic force microscopy (AFM) was employed and analyzed by multi-stage data quantification (MSDQ) that enables a statistically-relevant extrapolation of small-area features to the whole electrode area [50]. Parameters derived in primary AFM studies are given in **Table ST1**. Fig. 4a, b shows the surface topography of the as-prepared and plasma-treated Ni-Co-O samples.

The as-prepared sample has a higher maximum surface height of 3.7 µm, which reduces to 2.5 µm after plasma treatment. This visualization indicates that plasma treatment has affected the surface height variation, aligning with the previously discussed SEM top-view analysis. To further substantiate this observation, we analyzed two surface features: surface roughness (representing height variation) and homogeneity score (indicating the distribution of particles over the measured area of $100 \times 100\ \mu m^2$). These features are visualized using a 2D kernel plot in Fig. 4c. As expected, the reduction in surface roughness after plasma treatment correlates with an increased homogeneity score and it is clearly seen that the exposure to the N_2 plasma significantly alters the morphology and thus microstructure of the anodes.

2.2.2. *Cross-section and pore network of the Ni-Co-O layers*

To evaluate the differences in pore sizes between the as-prepared and plasma-treated samples, focused ion beam (FIB)-SEM was employed [51]. Fig. 5 shows cross-section images of the as-prepared, and the plasma-treated Ni-Co-O anodes, respectively. The pore coverage is defined as the portion of void space within the catalyst layer and is a crucial parameter that affects mass transport and access to active sites, directly influencing the catalytic performance of the layer [52]. The estimated pore coverage in the as-prepared and plasma-treated Ni-Co-O layers (both with thicknesses in the range 350–400 nm) are 11 and 14 %, respectively, along with a slight expansion of the coated layer after the plasma treatment. While a clear boundary with less pore density is observed at the interface between the substrate and the catalyst layer in the as-prepared films (highlighted by the horizontal dashed line in Fig. 5a), the plasma-treated films show a much smoother interface. We assume that the interaction of the deposited Ni-Co-O layers with the charged species in the plasma might have led to enhancing the contact between the coated layer and the substrate, likely induced by a layer rearrangement due to the energy input and the removal of the binder. This results in a more uniform layer and a smoother substrate-coated

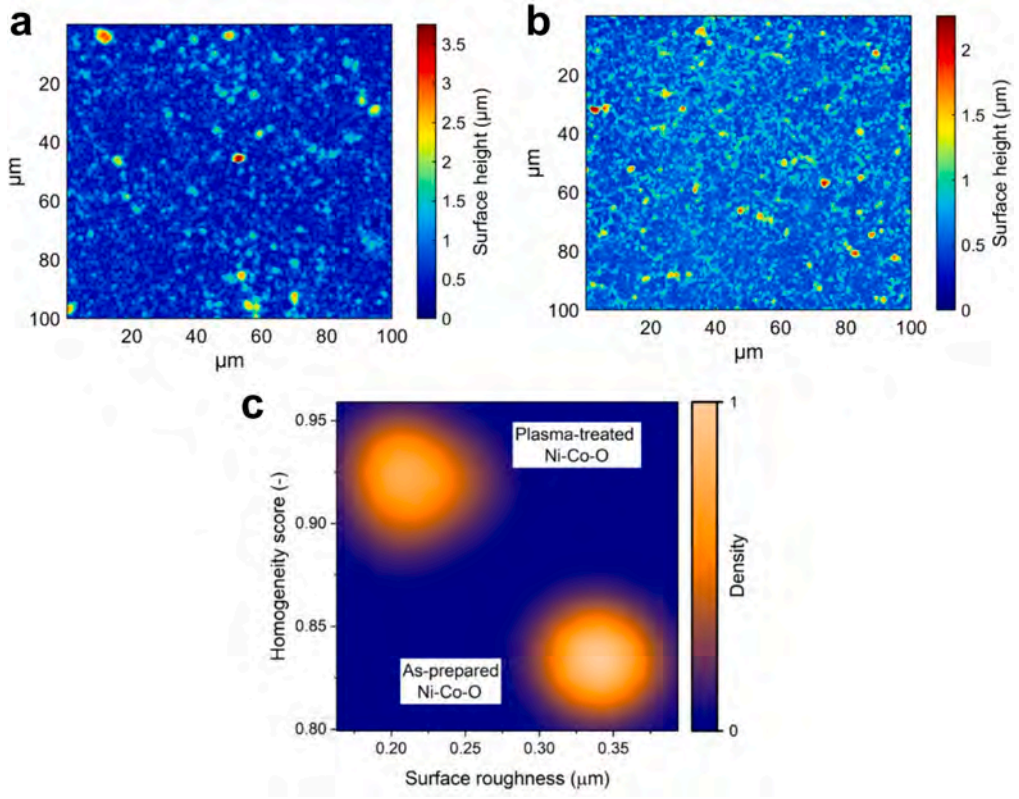

Fig. 4. AFM-MSDQ analysis: Topographical images of (a) as-prepared Ni-Co-O layer and (b) plasma-treated layer (c) 2D distribution of surface roughness and homogeneity score of as-prepared and plasma-treated anodes.

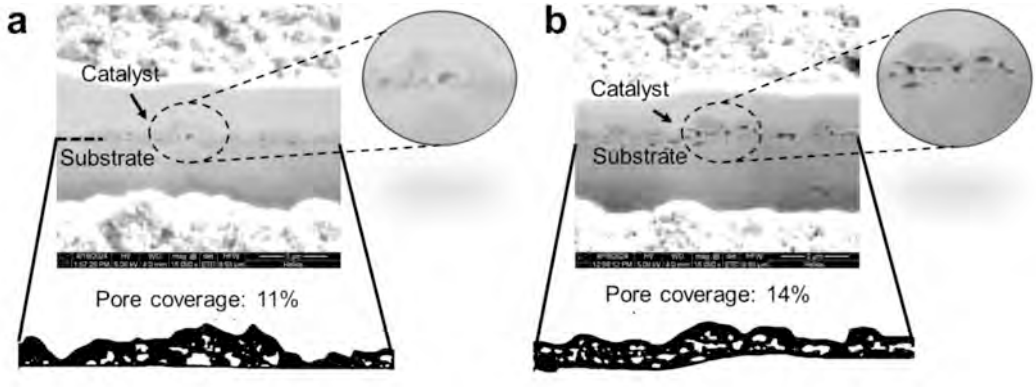

Fig. 5. FIB-SEM images showing the pore coverage in both (a) as-prepared and (b) plasma-treated Ni-Co-O layers. The horizontal dotted line in (a) indicates the boundary between the coated Ni-Co-O layer and the substrate. Zoom-in images are given for better clarity.

layer interface after the plasma treatment. The higher pore density in the plasma-treated Ni-Co-O films is also further validated by mercury intrusion porosimetry (MIP) measurements (**Fig. S7**) where in particular the abundance of pores of sizes starting from 200 nm is much higher in the plasma-treated layers. Altogether, the SEM-EDX, AFM and MIP analyses confirm the increased porosity and homogeneity of Ni-Co-O layers after plasma treatment. It is worth noting here that porous structures are expected to be beneficial for electrocatalytic water splitting as they can provide more surface active sites and enable easier mass diffusion [47].

2.2.3. *Crystal structure, surface composition, and wettability of Ni-Co-O layers*

After understanding the microstructure of the as-prepared and plasma-treated Ni-Co-O samples in detail, we now turn to the crystal structure and surface chemical state analysis of these layers. XRD was performed on the coated layers before and after the plasma treatment to identify changes in the structure compared to the Ni-Co-O powder

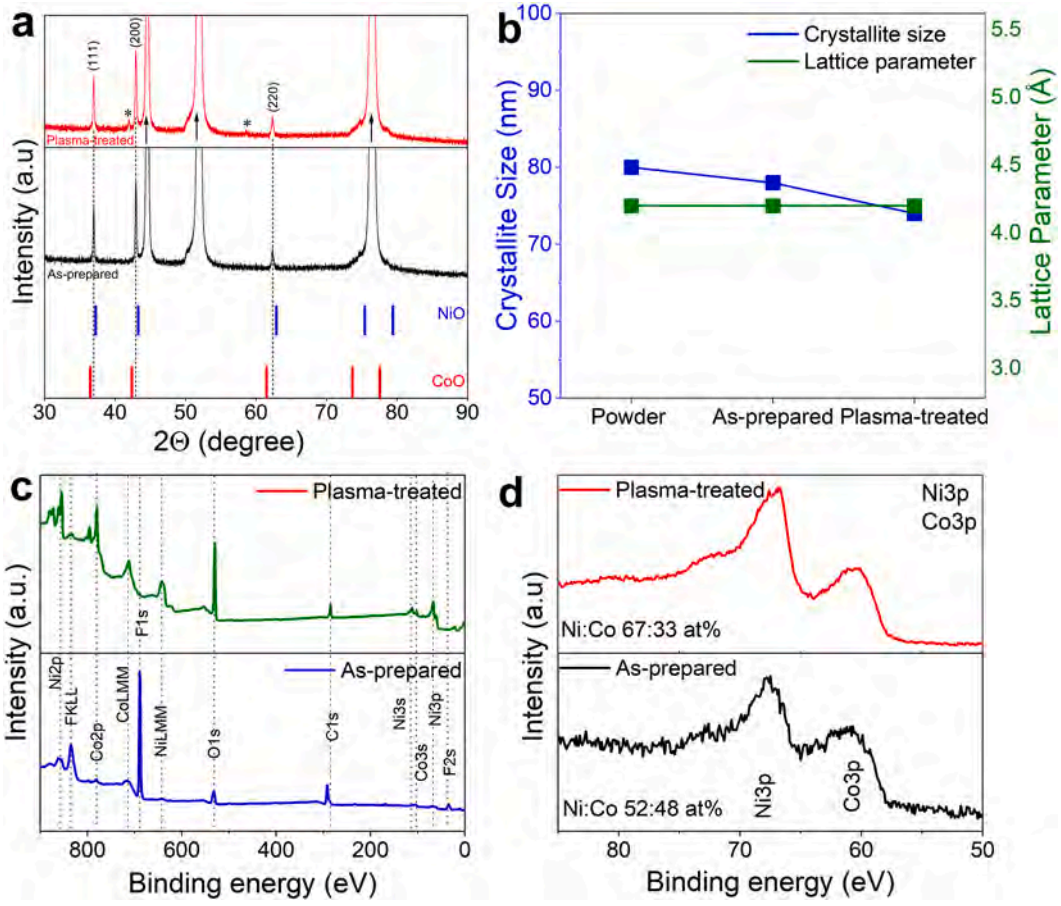

Fig. 6. (a) XRD spectra of the as-prepared and plasma-treated Ni-Co-O films with marked reflections corresponding to the Ni-Co-O FCC phase with reference patterns of NiO and CoO. The peaks marked with an asterisk match those of Ni_3N (ICDD# 82–5114). The reflections marked by the arrow correspond to the Ni substrate; (b) crystallite size and lattice parameter values derived from Rietveld refinement for both films; (c) XPS survey spectra with significant elemental peaks marked and (d) high-resolution XPS showing the Ni and Co3p region of the films.

precursor and due to the plasma treatment. Fig. 6a shows the XRD spectra of the as-prepared and plasma-treated Ni-Co-O layers on Ni plates. In general, the deposited Ni-Co-O layer exhibits the same crystal structure as the Ni-Co-O powder (Fig. S3a). In addition the reflections are observed at 2θ values of 44.5, 51.8, and 76.4° that can be assigned to the Ni substrate with an FCC structure ICDD# 04–0850. However, no apparent shift in the Ni-Co-O reflections on the layers was observed either in the as-prepared or plasma-treated layers, confirming that the initial bulk crystal structure of the powder is preserved in the spray-deposited films and after the plasma post-processing. While lattice parameters of the as-prepared and plasma-treated samples exhibit similar values, the crystallite size decreased after the plasma treatment from ~80 to 74 nm (Fig. 6b).

Additionally, new peaks appearing at 2θ = 42.01° and 58.65° in the plasma-treated layers (marked by *) can be assigned to nickel nitride (Ni_3N, ICDD# 82–5114). This indicates that nitrogen incorporation during plasma exposure, as detected by EDX measurements, leads (at least partially) to the formation of a nitride phase.

Since XRD is dominated by bulk information, we additionally performed XPS analysis on the as-prepared and plasma-treated Ni-Co-O layers to further explore plasma-induced surface chemical changes, which is highly relevant with respect to the application of the samples as electrocatalysts. Fig. 6c depicts XPS survey spectra of both as-prepared and plasma-treated Ni-Co-O layers. The most obvious observation is that the high-intensity F1s peak observed at ca. 690 eV in the as-prepared sample, attributed to the Fluorine in the Nafion binder (see the experimental section 2.6 in supplementary for details), is not present anymore in the plasma-treated sample. Simultaneously, the major C1s contribution in the as-prepared Ni-Co-O is assigned to -CF_2-CF_2- from Nafion which disappears after the plasma treatment (**Fig. S8**). Both changes indicate the surface removal of Nafion due to the plasma processing of the layer together with the incorporation of nitrogen. Due to the Fluorine-KLL auger interference (at ~835 eV) in the region of the Ni2p, features analysis of Ni and Co was restricted to the 3p region (Fig. 6d). The O, Ni and Co signals showed a significantly increased intensity after the plasma processing due to Nafion removal from the surface of the Ni-Co-O layer, further corroborating the finding of Nafion removal and the higher availability of Co and Ni sites on the surface upon plasma treatment. Though no obvious changes in the Ni3p and Co3p peak shape could be identified (**Fig. S9**), the XPS quantification of the surface composition showed a significant increase in the Ni:Co ratio after the plasma treatment. More than twice Ni (than Co) was found on the plasma-treated Ni-Co-O electrode surface. This can be caused by an enrichment of Ni at the surface of the Ni-Co-O, however, also additional contributions from the Ni substrate might play a role. Here, it is important to note that no significant nitrogen signal was detected in XPS on the plasma-treated Ni-Co-O, suggesting that the nitride detected by XRD arises from the bulk of the film rather than its surface. This interpretation is also consistent with previous studies, such as Ouyang et al. [53] who demonstrated the formation of Ni_3N through nitrogen plasma-treatment at elevated temperatures and short durations, wherein nitrogen species penetrate into the material and promote the formation of a bulk nickel nitride phase without necessarily modifying the outermost surface chemistry significantly. Similarly, Shalom et al. [54] reported the formation of Ni_3N via a solid-state reaction route with enhanced catalytic features attributed to subsurface nitride–hydroxide junctions. In our case, while the catalytic role remains to be explored, these findings lay the structural groundwork for future investigations of such plasma-induced nitride formation in Ni-based layered systems.

To compare the surface wettability of the as-prepared and plasma-treated Ni-Co-O layers, contact angle measurements were undertaken. The as-prepared Ni-Co-O electrode is characterized by a hydrophobic surface with contact angle ~118° (**Fig. S10**). In contrast, the contact angle after the layers underwent the N_2-plasma post treatment could not be detected due to their highly hydrophilic surface (with a contact angle ~0°). This pronounced hydrophilicity is mostly attributed to the changes that occurred in the surface morphology of the anodes together with the plasma-induced removal of the hydrophobic binder.

2.3. Electrochemical OER performance of Ni-Co-O anodes

After characterizing the morphology and physicochemical properties of the Ni-Co-O layers, their electrochemical performance as anodes for the OER was evaluated. **Fig. 7** compares the constant operation at 100 mA cm^{-2} for 2 h for as-prepared and plasma-treated Ni-Co-O anodes in a beaker cell configuration, using 1 M KOH as electrolyte with controlled Fe concentrations of 15 ppb and 110 ppb.

In the initial study with 15 ppb Fe in KOH (Fig. 7a), the coated electrodes demonstrated significantly higher activity, i.e. 113 ± 6 mV lower overpotential at the end of the chronopotentiometry (CP), compared to pristine Ni plate supports. This is logical, as pure Ni electrodes are mostly inactive in low Fe-electrolytes [55], while the addition of Co enhances the activity of Ni-based electrodes [54,55]. Furthermore, plasma-treated electrodes showed a notable improvement in the overall reproducibility of the measurement, with an 82 % reduction in standard deviation compared to the as-prepared electrodes, as indicated in the legend. This indicates that plasma treatment effectively altered the surface chemistry and irregularities, leading to more uniform and compact surface structures, which aligns with the surface topology discussed in section 2.2.1. Comparing the end-potential after two hours of CP analysis in the low iron-containing electrolyte, the plasma-treated Ni-Co-O (1.690 V vs. RHE) showed a ~ 10 mV reduction compared to as-prepared Ni-Co-O (1.698 V vs. RHE). Though small, this difference is significant, especially given the low standard deviation of the plasma-treated samples.

When tested with 110 ppb Fe in KOH (Fig. 7b), which is a more realistic iron concentration for alkaline electrolyzers at application-relevant conditions, the plasma-treated layers exhibited a significant lower overpotential after 2 h at 100 mA cm^{-2} (1.574 V vs. RHE), compared to the as-prepared Ni-Co-O anodes (1.617 V vs. RHE), as demonstrated in Fig. 7b. To further underpin these findings, measurements were also conducted in a flow cell configuration, where comparable trends were observed (**Fig. S11**), highlighting the robustness of the plasma-treated catalyst layers across different electrochemical test setups.

The same trend is corroborated by the activity cyclic voltamograms (CVs) for all samples (**Fig. S12a and b**). To better understand this behavior, the conditioning of the electrodes is depicted in Fig. 7c and d. For the electrolyte with low iron concentration (Fig. 7c), the charge passed during the oxidation and reduction of the electrodes is similar for the plasma-treated and the as-prepared sample. However, there is a significant charge-increase for the plasma-treated samples in the electrolyte with high iron concentration (Fig. 7d). The transferred charge can be linked to the development of an OER-active hydroxide layer during the phase transition from $Ni(OH)_2$ to NiOOH on the catalyst surface at higher potentials, resulting in the formation of a structure resembling Ni_xOOH/Co_xOOH [56]. Mattinen et al. [57] have shown that this oxide formation is dependent on the investigated material but also on the iron concentration in the electrolyte. Hence, we assume that plasma treatment favors the faster formation of Ni_x/Co_x-(Fe)OOH, compared to the as-prepared samples [58], which is shown in the larger oxidation and reduction peaks. The higher porosity of the plasma-treated samples could also facilitate the diffusion of the OH-, resulting in a faster conversion of the hydroxide. Apart from the increased charge transfer, we acknowledge an altered nature of the conditioning CVs before and after plasma treatment. However, a detailed analysis of the peak shift(s) due to plasma treatment would require *operando* surface-sensitive techniques and are hence beyond the scope of this work. Nevertheless, we attribute the observed variations to plasma-induced changes in surface morphology, defect structures, and Fe incorporation dynamics, which influence the electrochemical behavior of the Ni-Co surface.

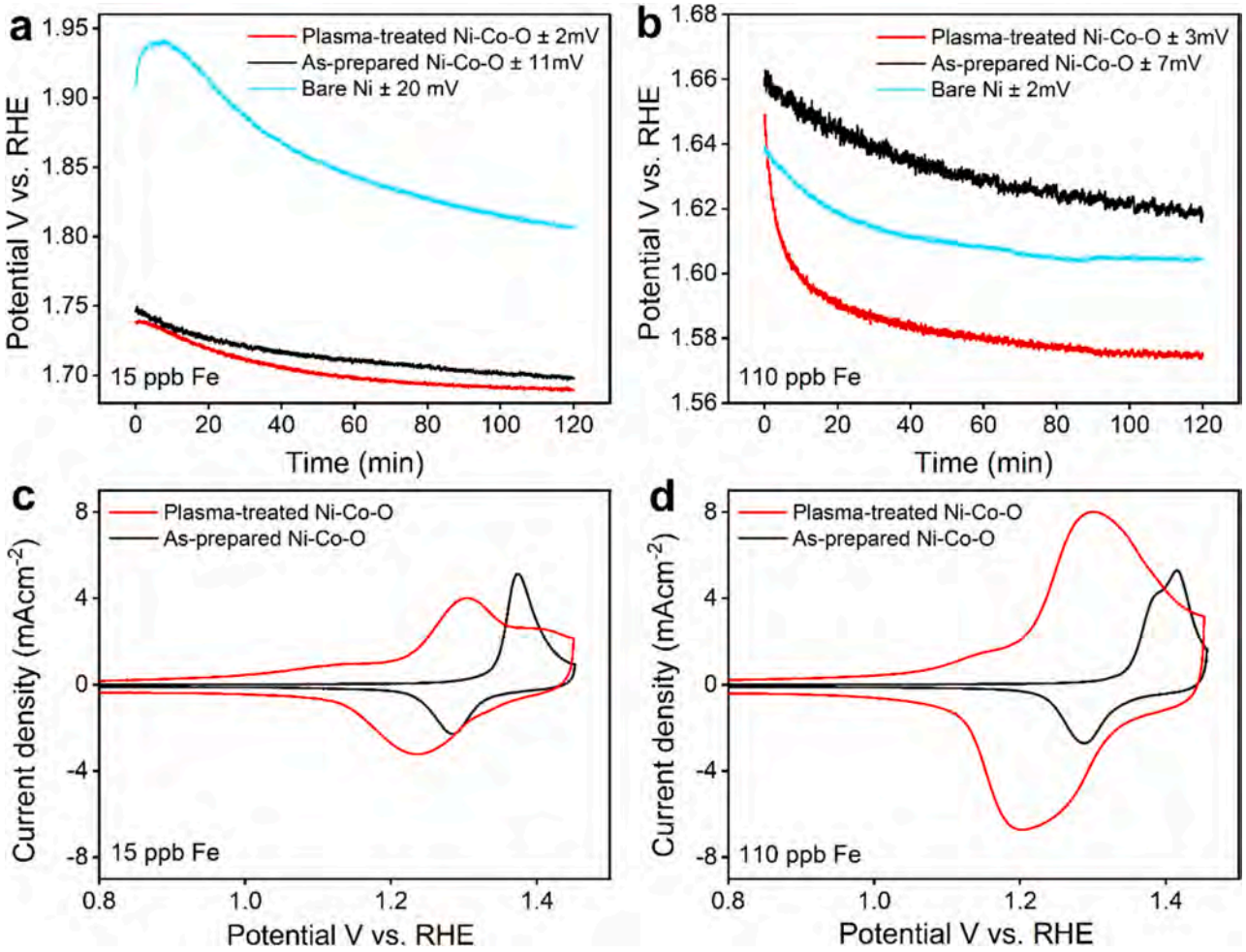

Fig. 7. (a) and (b): CP for 2 h at 100 mA cm^{-2} of as-prepared and plasma-treated Ni-Co-O electrodes measured in a beaker cell in 1 M KOH containing (a) 15 ppb and (b) 110 ppb Fe. Electrochemical conditioning of anodes in (c) 15 ppb and (d) 110 ppb containing 1 M KOH. Shown is the last of 50 cycles with a scan rate of 100 mV s^{-1} for a potential window of 0.2 V vs. RHE and 1.45 V vs. RHE.

Interestingly, in the electrolyte with higher iron concentration, the performance of the bare Ni support is better than the as-prepared samples (1.605 V vs. RHE after 2 h CP at 100 mA cm^{-2}, Fig. 7b). We assume that for the bare nickel, the active Ni_xFe_x-OOH species forms during the conditioning of the samples [59,60], due to the now elevated iron concentration in the electrolyte. At low iron concentrations, conditioning of nickel will still improve its activity, however the absolute activity remains significantly lower than in case of electrolytes with a high iron content [61]. This process could be faster for the bare nickel compared to the Ni-Co-O, due to the already oxidized state of the powder-based anodes, needing more time for the restructuring of the surface into a similar $Ni_x/Co_x/Fe_x$ – OOH species.

In light of these considerations, single-cell measurements were conducted at 80 °C under recirculation of the 1 M KOH (150 ppb Fe) electrolyte (**Fig. S13**). Notably, the plasma-treated anode outperforms the as-prepared sample as expected, e.g. 34 mV lower overpotential at 500 mA cm^{-2} (Fig. S13a). In the short-term stability test of the plasma-treated sample, an initial deactivation is noted (Fig. S13c), however, this initial deactivation is totally recovered after replacing the electrolyte to the new KOH solution, demonstrating excellent stability of catalyst layers in single-cell operation (detailed information is available in the supporting information discussion provided on page 11).

It is important to consider that the electrochemical active surface area (ECSA) of as-prepared and plasma-treated samples may differ due to their distinct surface morphologies (Fig. 3b, c), making an evaluation of the ECSA highly relevant. To investigate this, ECSA measurements were performed for the beaker cell experiments using rapid CV cycling, as described in the literature [56]. However, the capacitance values obtained should be interpreted with caution, as the measured double-layer charging may overlap with effects such as continuous Ni and Co oxidation. Despite this limitation, the capacitance values (**Table ST2**) showed a clear increase for the plasma-treated samples compared to as-prepared ones. While we refrain from directly correlating this to larger ECSAs, the data qualitatively suggests that plasma treatment induces noticeable morphological changes.

So far, we hypothesize that plasma treatment favors the formation of hydroxides, improves gas bubble transport due to an altered pore structure, removes Nafion from the surface, and induces defects, thereby exposing more active sites for the reaction. The plasma-induced removal of organic binders, particularly Nafion, eliminates potential mass transport limitations and enhances the electrochemically accessible surface area. This approach is beneficial for both traditional AWE and more advanced AEMWE configurations (without catalyst coated membranes) as demonstrated in this work.

Additionally, as previously discussed, nitrogen incorporation during plasma treatment also likely plays a role in altering the catalytic performance. For instance, some previous studies have reported that Ni_3N may act as an effective precursor for hydrous oxide formation, facilitating faster generation of OER-active (oxy)hydroxide species by modifying lattice strain and promoting oxygen vacancies [62,63]. However, we assume that this effect is less significant in our samples due to the absence of the N-species on the surface which is in contact with

the electrolyte during the reaction. While it is well known that iron incorporation enhances the OER performance of Ni-based catalysts, our study explores how plasma treatment modifies the Ni-Co-O surface and its interaction with Fe in the electrolyte. We demonstrate that plasma treatment leads to enhanced catalytic performance and reproducibility by promoting OER-active (oxy)hydroxide formation. Although the absolute OER performance of the commercial Ni-Co-O is below that of advanced, recently synthesized electrode materials, we were able to uncover how plasma treatment influences surface properties and significantly reduced overpotential. Moreover, all measurements were conducted on plate electrodes, which inherently exhibit lower performance compared to realistic support materials, such as felts or meshes. Nonetheless, our findings can likely be applicable also for different support geometries. Altogether, this demonstrates the role of the plasma treatment in enhancing the catalytic performance and – independent of the test setup, – underscores the effectiveness of plasma-treated Ni-Co-O anodes for the alkaline OER.

To better understand the impact of plasma treatment of Ni-Co-O on the OER performance, we conducted X-ray absorption spectroscopy (XAS) measurements on pre- and post-electrochemical samples, along with *operando* Raman analysis. These results are discussed in the following section.

2.4. XAS and operando Raman measurements on Ni-Co-O anodes

Since the XPS analysis was complex for the Nafion-containing as-prepared Ni-Co-O films, to further evaluate the changes of the near-surface electronic structure induced by the plasma treatment, we applied a multi-element analysis by XAS in total electron yield (TEY) and total fluorescence yield (TFY) mode at the N, O and F K-edge, as well as at the Fe, Co and Ni L-edges. To obtain knowledge about further surface changes induced during electrochemistry, samples were also analyzed after electrochemical characterization. Comparison of Ni and Co L-edge spectra with different reference spectra demonstrates that prior to the plasma treatment, Ni and Co were both mainly in a 2+ oxidation state (**Figs. S14 and S15**). The main features of the O K-edge spectrum of the plasma-treated sample coincide with the main features of the Ni- and Co-oxide reference spectra (Fig. 8). In the spectrum of the as-prepared sample, these features are superimposed by the contributions of the Nafion binder. These findings are in line with the presence of the mixed oxidic rock salt Ni-Co-O phase in both, the as-prepared and plasma-treated layers. Spectroscopic changes of the Ni and Co L-edges after plasma treatment indicate partial oxidation of Ni^{2+} to Ni^{3+} (indicated by a slight intensity increase at 854.6 eV, Fig. S14) and Co^{2+} to Co^{3+} (indicated by a notable intensity decrease at 776.9 eV, 778.2 eV, and 778.6 eV accompanied with an intensity increase at 780.2 eV, Fig. S15). The Ni oxidation is also reflected in the feature at 528.9 eV in the O K-edge spectra [64–66].

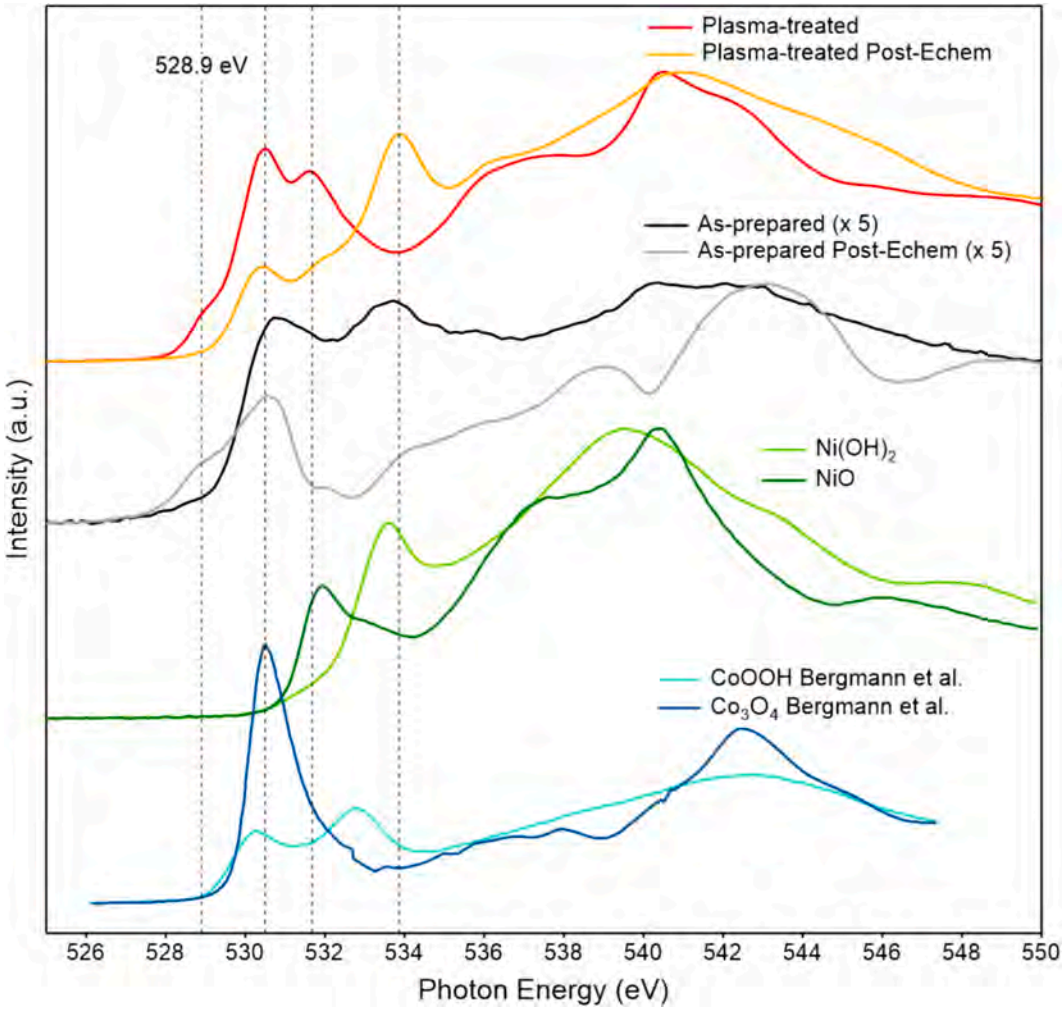

Fig. 8. Averaged O K-edge spectra of the as-prepared and the plasma-treated samples before and after the electrochemical treatment, normalized to their maximum in comparison with reference spectra. The spectra of the as-prepared samples were scaled by a factor of five for better comparison. The literature spectra are taken from Bergmann et al. [66].

Furthermore, TEY XAS allows us to examine differences in the near-surface electronic structure present after the electrochemical characterization of the material between the plasma-treated and as-prepared Ni-Co-O. The most significant changes of the O K-edge spectra indicate a partial transformation of the Ni-Co-O phase in both samples into a Ni-Co hydroxide phase, as demonstrated by comparison with reference spectra. Such a transformation is also reflected in the Ni and Co L-edge spectra (**Fig. S16-S19**). Along with the structural transformation, the Ni and Co species at the surface of the as-prepared sample become partially oxidized after the electrochemical characterization (Fig. S16 and Fig. S18). This partial oxidation is particularly pronounced for Co.

In contrast, in the plasma-treated sample, in which Ni^{3+} and Co^{3+} contributions were detected also before the electrochemical treatment, the Ni and Co oxidation states appear to be slightly reduced after applying the electrochemical protocol (Fig. S17 and Fig. S19). The lower metal oxidation states after electrochemical treatment probably indicate better reversibility of the metal oxidation taking place during OER. This is an indication of structural changes in the active phase and might be correlated with the enhanced Ni/Co-ratio on the surface of the plasma-treated sample observed via XPS. Such compositional changes influence the OER activity [67] and may contribute to the observed differences in electrochemical performance. Most interestingly the Co oxidation state prior to and post electrochemistry appears more stable in the plasma-treated sample compared to the as-prepared anode, which could be explained by the lower amount of Co at the surface, while rather being stabilized in the bulk, and thus less involvement in the surface reactions.

Another important observation was made at the Fe L-edge, where a small Fe L-edge contribution can be seen only in the spectra of the as-prepared sample indicating some Fe impurities to be present on the surface, before applying the electrochemical protocol, which disappear after the plasma treatment (**Fig. S20**). After the electrochemical treatment only an apparent oxidation but no obvious changes in the Fe L_3 edge intensity were observed for the as-prepared sample while the Fe signal in the plasma-treated sample showed a strong increase significantly exceeding that of the as-prepared anode. This indicates a facilitated Fe-uptake for the plasma-treated Ni-Co-O compared to the as-prepared sample. This is perfectly in line with the observed higher electrocatalytic activity, as the implementation of Fe increased the activity of Ni-Co catalysts severely [68]. The Fe spectra measured in the plasma treated sample after the electrochemical protocol resemble the shape of Fe^{3+} species (**Fig. S20** and **S21**) and likely stem from the Fe in the utilized KOH.

Further, N K-edge TFY spectra suggest a partial nitrogen incorporation resulting from the N_2 plasma treatment. This nitrogen remains in the sample after the electrochemical treatment and shows features in line with the formation of nitride species (**Fig. S22**). Surface sensitive TEY measured at the N K-edge did not yield conclusive N K-edge spectra, which is in line with XPS results, showing also no nitrogen feature. Therefore, we assume a major part of the implemented nitrogen species to be present in the bulk rather than at the surface, which is also in agreement with previously discussed XPS measurements. A detailed evaluation of the electronic structure of the nitrogen species, however, remains challenging because the N K-edge spectrum appears to be distorted due to an intensity modulation induced by a Si_3N_4 window, which is implemented in the utilized setup. Finally, in agreement with the EDX results, the intensity of the F K-edge resonance almost completely vanishes after plasma treatment indicating successful removal of the Nafion binder (**Fig. S23**).

In total, the XAS measurements on the as-prepared and plasma-treated Ni-Co-O layers before and after electrochemical tests indicated significant differences as mentioned above. To gain more insight into the dynamics of the phase transformations, we conducted *operando* Raman measurements. For the *operando* Raman measurements, both samples were first conditioned using a cyclic voltammetry (CV) protocol (see Experimental section in supplementary 2.12 for details) prior to recording the Raman spectra. Raman spectra were then collected at selected potentials chosen based on the features observed from a low scan rate CV scan (**Fig. S24**) to identify and compare dynamic changes in the active phases in these two electrodes.

Fig. 9 shows the *operando* Raman measurements conducted on the (a) as-prepared and (b) plasma-treated Ni-Co-O electrodes. Raman spectra of the as-prepared Ni-Co-O layer exhibit two major Raman bands located around 460 and 538 cm^{-1} at an applied potential of 1.0 V vs. RHE (Fig. 9a) which can be assigned to Ni-O vibrations in $Ni(OH)_2$ [69]. During the anodic scan, these bands are consistently observed with a small blue shift with increasing the potential up to 1.48 V vs. RHE which is reversible upon applying the reductive potentials. This reproducible blue shift during the anodic scan points to the shortening of the metal-oxygen bond length and thus an increase of the polarizability due to the change of the electron cloud distribution within the catalyst layer [70].

In contrast, after the plasma treatment, there is only a broad Raman band observed starting at 470 cm^{-1} at 1.0 V (Fig. 9b). When the potential is stepwise anodically increased, a second peak emerges at 541 cm^{-1} which further increases the intensity at the OER onset potential of 1.5 V. The Raman band at 541 cm^{-1} disappears again during the cathodic scan below 1.3 V. It is reasonable in this case to expect the existence of (oxy-)hydroxy species such as NiOOH and/or CoOOH forming before the OER. It has to be noted, that the potentials were not scanned to a region where OER starts – to avoid distortions due to bubble formation – and the Raman spectrum of the active phase of the catalyst during OER might still differ from our results. However, Yang et al. reported the broadening of the Ni-OOH species derived from $Ni(OH)_2$ and a shoulder peak along with the 551 cm^{-1} band to the co-existing Ni and Co-OOH in NiCo double hydroxides under applied potentials in 1 M KOH [71]. Similarly, also in our *operando* investigations, a broader nature of the Raman bands is observed in the plasma-treated electrode compared to the more defined bands observed in the as-prepared Ni-Co-O layer suggesting that the contribution of different phases varies between the two samples during electrochemical testing.

The emergence of the Raman peak at approximately 610 cm^{-1} at lower potentials (1.0 V vs. RHE) after nitrogen plasma treatment may in addition reflect the more facile formation of cobalt oxyhydroxide phases (CoOOH) or defect-rich cobalt oxides. Here, the plasma treatment could induce structural defects and vacancies, increasing surface Co accessibility and stabilizing transient intermediate Co species. Such cobalt-based surface intermediates could be advantageous for enhancing catalytic activity and stability during OER. Still, an accurate assignment of the Raman bands in each case is challenging and the focus is therefore put on the significantly different potentiodynamic behavior of the spectra for the as-prepared and plasma-treated electrodes where the latter shows a prominent reversible phase change and a much more “flexible nature” in comparison to the as-prepared Ni-Co-O under similar applied potentials, which might also be beneficial for activity improvement.

Finally, taken all data together, it is justified to conclude that several factors contribute to the enhanced activity of the plasma-treated Ni-Co-O electrodes:

(i) The surface morphology of the plasma-treated Ni-Co-O is significantly different from that of the as-prepared layers in such a way that plasma-treatment induces a more homogeneous surface with a larger share of primary particles and thus a higher surface area that is exposed to the electrolyte.
(ii) The plasma treatment removed most of the organic species from the surface of the electrodes, thus making the active material more accessible to the electrolyte. Both, the more favorable surface morphology and binder removal directly affect the electrochemical active surface area and density of active sites.
(iii) XRD and TFY suggest that plasma-treatment led to the formation of a Ni_3N phase in the bulk of the Ni-Co-O layers, while XPS and TEY show that N is not present on the surface. These N-species

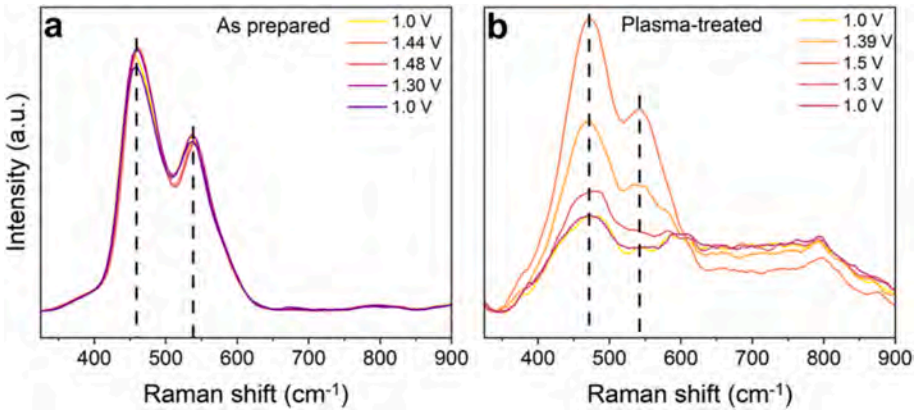

Fig. 9. *Operando* Raman measurements on (a) as-prepared and (b) plasma-treated Ni-Co-O layers under constant applied potentials in chronoamperometry measurements.

incorporated in the bulk structure might have an influence on the final catalytic performance.

(iv) The plasma-treated Ni-Co-O films exhibited a highly hydrophilic surface compared to the hydrophobic nature of the surface in the as-prepared films, due to the changes induced in the surface morphology and surface binder removal.

(v) XAS studies highlight a higher Fe-uptake by the plasma-treated electrode than the as-prepared Ni-Co-O, together with differences in the surface metal-oxide species between the two types of anodes. Additionally, XAS results indicate nitrogen incorporation into the bulk phase due to the plasma processing.

(vi) Both XAS and *operando* Raman studies underline a more reversible oxidation behavior in the plasma-treated layers when used as anodes in OER which further influences the activity.

Disentangling the individual effects of each of these phenomena on the OER performance is beyond the scope of this work, however, our findings pave the way for extensive future research in this direction. The coherent workflow for multi-stage anode development enabled this systematic investigation, starting from in-depth powder analysis through ink formulation to electrode coating, surface treatment by N_2 plasma, and subsequent application of the electrodes as OER catalysts (Fig. 10). Finally, the effectiveness of the plasma post treatment on the

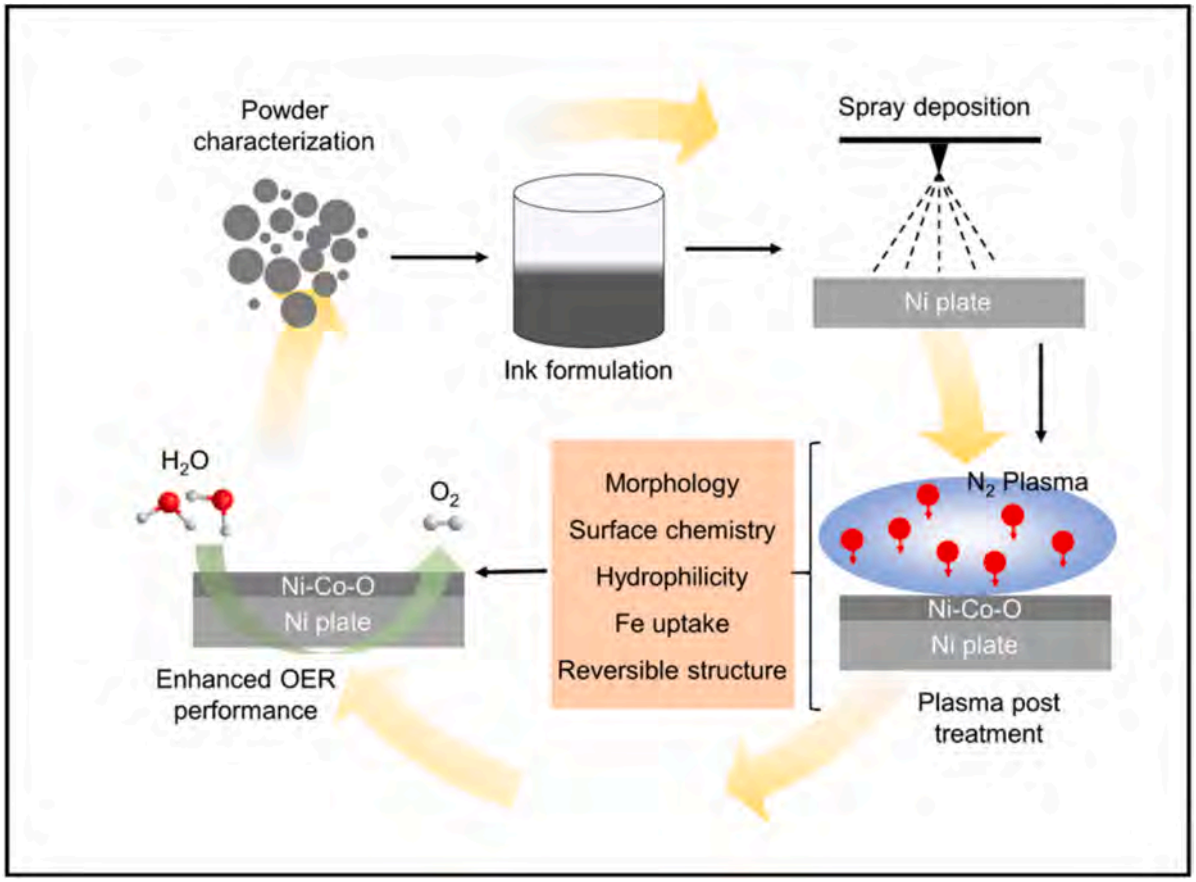

Fig. 10. Schematic representation of the coherent workflow cycle starting from the initial powder selection and characterization through ink formulation, catalyst deposition, and plasma post treatment-induced changes, leading to the observed, significantly enhanced OER performance.

OER performance of spray-coated Ni-Co-O is analyzed and demonstrated to be an efficient, potentially scalable way to obtain binder-free, potent anodes, even from commercial materials, by proper processing.

3. Conclusion

In conclusion, we have demonstrated a systematic approach to characterize transition-metal-oxide catalysts from their initial powder state along the process chain from catalyst inks to coated layers, enabling in-depth understanding, comparability, and a multistage optimization-pathway using Ni-Co-O as a model system. At each stage, the material was meticulously analyzed using a comprehensive set of analytical tools, and insights into powder properties, ink formulation, and layer characteristics were leveraged to further refine the system. We chose a commercial Ni-Co-O powder as an example material and first developed a stable catalyst ink by evaluating its HSP. Subsequently, Ni-Co-O films were obtained through spray coating onto Ni plate substrates that were post-processed by means of N_2 plasma to modify the active layer in terms of morphology, pore structure, wettability, and surface chemistry. The plasma treatment significantly altered the Ni-Co-O films, resulting in a distinct surface morphology and increased accessibility of the active material by removing organic species. Characterization of the plasma-treated Ni-Co-O layers, first, unraveled anodes with a minor Ni_3N phase within the bulk and a highly hydrophilic surface, facilitating interaction with the electrolyte. Second, XAS studies further confirmed differences in the surface metal-oxide composition by pointing toward nitrogen incorporation upon plasma treatment and evidencing a higher Fe uptake from the electrolyte during OER. Finally, *operando* Raman studies showed a more reversible oxidation behavior in the case of plasma-treated layers. Overall, these modifications contributed to enhanced OER performance of the Ni-Co-O anodes in both half-cell and single-cell operations due to the plasma post-treatment with enhanced reproducibility.

The achieved, significant gain in the finally obtained OER performance of the generated anodes underlines the necessity for a thorough continuous characterization of catalysts throughout the entire process chain, highlights the decisive role of plasma post-treatment in further optimizing the anode layer properties, and explains why it is so effective. Rather than focusing on only singular aspect of the anode development, we provide a comprehensive picture where each stage of processing significantly affects the properties of the final anodes and thereby the overall OER performance.

Considering that the plasma post-treatment leads to the removal of the Nafion binder and induces surface morphological changes, we believe that our approach could be also transferred to other similar transition-metal-based systems where material properties can be fine-tuned to achieve high-performing, binder-free, and cost-effective catalysts for both AWE and AEMWE. However, it should be noted that although the plasma-induced binder removal might be generally applicable to a wide range of materials, the associated modifications to the morphology and surface chemical properties might be different for each system and require detailed individual examination for every new material.

4. Experimental section

4.1. Materials

Commercial Ni-Co-O nanopowder, (99 %, CAS number 58591–45-0) was purchased from Sigma-Aldrich. Deionized water (>18.1 MΩ) was obtained from a Milli-Q system. Nafion™ perfluorosulfonic acid (PFSA) 5 % dispersions – D521, which was used as the binder, was obtained from Ion Power GmbH. For the spray deposition of the Ni-Co-O, nickel plates (Ra < 0.1, 99.2 %, HMW Hauner, pre-cut into 1 × 1 cm^2 pieces) were used as substrates.

4.2. Dispersion preparation and sedimentation analysis

4.2.1. Hansen solubility parameters

Dispersions were obtained by sonicating the Ni-Co-O powder in probe liquids with an ultrasonic homogenizer (Branson). The probe liquids were selected according to the two-step procedure developed by Amin et al. [36]. In the first step, EtOH, DMF, and THF were used to identify liquids that form good dispersions with the Ni-Co-O powder. Based on the stability of the dispersion in the first step, additional probe liquids were screened in the second step and the resulting probe liquid list was used to make the ranking for HSP determination according to Süß et al. [37].

Analytical centrifugation was used to sediment the dispersions using artificial gravity. The dispersions were filled into measurement cells with 2 mm path length and inserted into a LUMisizer LS651 (LUM GmbH) analytical centrifuge and centrifuged at 2000 rpm for 20 h at 20 °C using 410 nm wavelength light. After the measurement, transmission fingerprints were generated by resolving the measurement time and position. Furthermore, transmittograms were plotted from the sedimentation data as well as described by Bapat et al. [35].

4.2.2. Ink formulation

The catalyst ink was prepared in the following way: first 30 mg of the Ni-Co-O powder was measured into a centrifuge tube followed by the addition of either 30 mL water or 30 mL of an EtOH:water mixture (volume ratio 1:1 r.t.p). The so-obtained suspension was homogenized by applying 18 min of probe sonication (Hielscher UP200Ht, Germany, ultrasonic homogenizer operating at 26 kHz, 20 % amplitude) [39] in three equal intervals of 6 min. Before commencing the last round of sonication, a small amount of Nafion (20 wt%) was also added to the mixture. During the probe sonication, the ink was kept inside an ice bath to avoid evaporation.

4.3. Spray coating of Ni-Co-O layers

Ni-Co-O layers were generated by spray coating the Ni-Co-O ink onto Ni plate substrates. Prior to the spray deposition, nickel plates were cleaned ultrasonically first with de-ionized water, followed by 1 M HCl solution, deionized water, ACE, and IPA to remove any surface contaminants. An ultrasonic spray coater (Sono Tek Co., NY) with an air pressure of 30 mbar was used. The Ni plates were heated to 150 °C during spray deposition to facilitate solvent evaporation from the substrate surface. All inks were applied at a constant flow rate of 0.4 mL min^{-1}, with a total of 20 layers deposited. To ensure a uniform coating, the first layer was sprayed horizontally across the plate. For subsequent layers, the spray direction was alternated by 90 degrees, with each new layer applied perpendicularly to the previous one. This alternating pattern was repeated until all 20 layers were deposited. Approximately 8 mL of ink was sprayed onto the Ni substrates, resulting in an average catalyst loading of ~120 μg cm^{-2}, as confirmed gravimetrically.

4.4. Plasma post-treatment on coated Ni-Co-O layers

After depositing Ni-Co-O films onto Ni plate substrates, the samples underwent a post-treatment in a microwave plasma reactor. The plasma setup used in this work is a custom-built reactor, specifically designed to incorporate high flexibility in processing capabilities as well as a high adaptability for later scaling and compatibility with industrial applications. A commercially available 2.45 GHz IPLAS CYRANNUS I-6″ plasma resonator is used as the basis for the reactor. The samples were positioned on a glass sample holder within the reactor. To eliminate contaminants, the reactor was first evacuated. Nitrogen gas was then introduced into the reactor using mass flow controllers while maintaining the vacuum pump at full speed. A gas flow rate of approximately 400 sccm was carefully adjusted to stabilize the reactor pressure at 1 mbar. With a microwave power set to 1 kW, the plasma was ignited. *E-H*

tuners were employed to achieve the desired plasma mode and to minimize the reflected power. After a treatment duration of 10 min, the plasma treatment was stopped. The gas supply was subsequently shut off, and the reactor was once again evacuated to remove any residual gas. Finally, the reactor was vented, allowing for the safe removal of the treated samples. More details on the plasma treatment can be found in [49].

4.5. Characterization methods

The Ni-Co-O powder, as-prepared and plasma-treated films were characterized in detail using a number of analytical tools of which detailed information can be found in the supplementary data (section 2). The specific details of the electrochemical analysis conducted both in the beaker (**Fig. S25**) and flow cell (**Fig. S26**) configurations are also provided in supplementary information (section 2.10).

CRediT authorship contribution statement

Vineetha Vinayakumar: Writing – review & editing, Writing – original draft, Visualization, Validation, Supervision, Methodology, Investigation, Formal analysis, Data curation, Conceptualization. **Timo Wagner:** Writing – review & editing, Visualization, Validation, Methodology, Investigation, Data curation. **Christian Marcks:** Writing – review & editing, Visualization, Validation, Methodology, Investigation, Formal analysis, Data curation. **Jacob Johny:** Writing – review & editing, Writing – original draft, Visualization, Validation, Methodology, Investigation, Formal analysis, Data curation, Conceptualization. **Garlef Wartner:** Writing – review & editing, Writing – original draft, Visualization, Validation, Methodology, Investigation, Formal analysis, Data curation, Conceptualization. **Ahyoun Lim:** Data curation, Formal analysis, Investigation, Methodology, Validation, Visualization, Writing – original draft, Writing – review & editing. **Marc F. Tesch:** Writing – review & editing, Writing – original draft, Visualization, Validation, Methodology, Investigation, Formal analysis, Data curation, Conceptualization. **Ioannis Spanos:** Writing – review & editing, Writing – original draft, Visualization, Validation, Methodology, Investigation, Formal analysis, Data curation, Conceptualization. **Aliakbar Ghafari:** Writing – review & editing, Visualization, Validation, Investigation, Formal analysis, Data curation. **Adarsh Jain:** Writing – review & editing, Writing – original draft, Visualization, Validation, Methodology, Investigation, Formal analysis, Data curation. **Oleg Prymak:** Writing – review & editing, Writing – original draft, Visualization, Validation, Methodology, Investigation, Formal analysis, Data curation. **Ignacio Sanjuán:** Writing – review & editing, Writing – original draft, Visualization, Validation, Methodology, Investigation, Formal analysis, Data curation. **Ahammed Suhail Odungat:** Writing – review & editing, Writing – original draft, Visualization, Validation, Methodology, Investigation, Formal analysis, Data curation. **Osama Anwar:** Writing – original draft, Visualization, Validation, Methodology, Investigation, Formal analysis, Data curation. **Mohit Chatwani:** Writing – review & editing, Visualization, Validation, Methodology, Investigation, Formal analysis. **Aneeta Jose:** Writing – review & editing, Visualization, Validation, Methodology, Investigation, Formal analysis. **Vimanshu Chanda:** Writing – review & editing, Visualization, Validation, Methodology, Investigation, Data curation. **Axel Knop-Gericke:** Writing – review & editing, Visualization, Validation, Supervision, Methodology, Investigation, Formal analysis. **Corina Andronescu:** Writing – review & editing, Writing – original draft, Visualization, Validation, Supervision, Methodology, Conceptualization. **Anna K. Mechler:** Writing – review & editing, Writing – original draft, Visualization, Validation, Supervision, Investigation, Funding acquisition, Conceptualization. **Nicolas Wöhrl:** Writing – review & editing, Writing – original draft, Visualization, Validation, Supervision, Methodology, Investigation, Formal analysis, Conceptualization. **Doris Segets:** Writing – review & editing, Writing – original draft, Visualization, Validation, Supervision, Resources, Project administration, Methodology, Investigation, Funding acquisition, Formal analysis, Conceptualization.

Declaration of competing interest

The authors declare that they have no known competing financial interests or personal relationships that could have appeared to influence the work reported in this paper.

Acknowledgements

The authors acknowledge the financial support from the Federal Ministry of Research, Technology and Space (BMFTR project “Prome-tH_2eus”, FKZ 03HY105F, 03HY105E, 03HY105A). We are also grateful for the support provided by the Mercator Research Center Ruhr (MERCUR.Exzellenz, ‘DIMENSION’ Ex-2021-0034). This work was also funded by the UDE Postdoc Seed Funding. IS and CA acknowledge the support of the Ministry of Culture and Science of the State of North Rhine-Westphalia (PB22-019). OA and DS acknowledge the Mat4Hy consortium for cooperative support. Open Access funding was facilitated and organized by Projekt DEAL. We extend our thanks to M. Heidelmann from the Interdisciplinary Center for Analytics on the Nanoscale (ICAN) for their valuable assistance. John-Tommes Krzeslack, Lukas Pielsticker, and Walid Hetaba from MPI-CEC are greatly acknowledged for their support with the XPS analysis. XAS Measurements were carried out at the ISSIS beamline and at the LiXEdrom endstation at the U49-2 PGM-1 beamline, both allocated at the BESSY II electron storage ring operated by the Helmholtz-Zentrum Berlin für Materialien und Energie.

Appendix A. Supplementary data

Supplementary data to this article can be found online at https://doi.org/10.1016/j.cej.2025.167169.

Data availability

The data that support the findings of this study are openly available in Zenodo at https://doi.org/10.5281/zenodo.16949835

References

[1] H. Tüysüz, Alkaline water electrolysis for green hydrogen production, Acc. Chem. Res. (2024) 697–710.
[2] Y. Zuo, S. Bellani, M. Ferri, G. Saleh, D.V. Shinde, M.I. Zappia, R. Brescia, M. Prato, L. De Trizio, I. Infante, High-performance alkaline water electrolyzers based on Ru-perturbed cu nanoplatelets cathode, Nat. Commun. 14 (1) (2023) 4680.
[3] M. Chatenet, B.G. Pollet, D.R. Dekel, F. Dionigi, J. Deseure, P. Millet, R.D. Braatz, M.Z. Bazant, M. Eikerling, I. Staffell, Water electrolysis: from textbook knowledge to the latest scientific strategies and industrial developments, Chem. Soc. Rev. 51 (11) (2022) 4583–4762.
[4] Y.-C. Zhang, C. Han, J. Gao, L. Pan, J. Wu, X.-D. Zhu, J.-J. Zou, NiCo-based electrocatalysts for the alkaline oxygen evolution reaction: a review, ACS Catal. 11 (20) (2021) 12485–12509.
[5] M. Yue, H. Lambert, E. Pahon, R. Roche, S. Jemei, D. Hissel, Hydrogen energy systems: a critical review of technologies, applications, trends and challenges, Renew. Sust. Energ. Rev. 146 (2021) 111180.
[6] Q. Wang, Y. Cheng, H.B. Tao, Y. Liu, X. Ma, D.S. Li, H.B. Yang, B. Liu, Long-term stability challenges and opportunities in acidic oxygen evolution electrocatalysis, Angew. Chem. 135 (11) (2023) e202216645.
[7] Z.J. Xu, Transition metal oxides for water oxidation: all about oxyhydroxides? Sci. China Mater. 63 (1) (2019) 3–7.
[8] N. Wen, X. Jiao, Y. Xia, D. Chen, Electrocatalysts for the oxygen evolution reaction: mechanism, innovative strategies, and beyond, Materials Chemistry Frontiers 7 (20) (2023) 4833–4864.
[9] A. Higareda, D.L. Hernández-Arellano, L.C. Ordoñez, R. Barbosa, N. Alonso-Vante, Advanced electrocatalysts for the oxygen evolution reaction: from single-to multielement materials, Catalysts 13 (10) (2023) 1346.
[10] M. Plevova, J. Hnat, K. Bouzek, Electrocatalysts for the oxygen evolution reaction in alkaline and neutral media. A comparative review, J. Power Sources 507 (2021) 230072.
[11] M.-I. Jamesh, X. Sun, Recent progress on earth abundant electrocatalysts for oxygen evolution reaction (OER) in alkaline medium to achieve efficient water splitting–a review, J. Power Sources 400 (2018) 31–68.

[12] X. Xie, L. Du, L. Yan, S. Park, Y. Qiu, J. Sokolowski, W. Wang, Y. Shao, Oxygen evolution reaction in alkaline environment: material challenges and solutions, Adv. Funct. Mater. 32 (21) (2022) 2110036.
[13] S. Cherevko, S. Geiger, O. Kasian, N. Kulyk, J.-P. Grote, A. Savan, B.R. Shrestha, S. Merzlikin, B. Breitbach, A. Ludwig, Oxygen and hydrogen evolution reactions on Ru, RuO2, Ir, and IrO2 thin film electrodes in acidic and alkaline electrolytes: a comparative study on activity and stability, Catal. Today 262 (2016) 170–180.
[14] H. Sun, W. Jung, Recent advances in doped ruthenium oxides as high-efficiency electrocatalysts for the oxygen evolution reaction, J Mater Chem A 9 (28) (2021) 15506–15521.
[15] Y. Lee, J. Suntivich, K.J. May, E.E. Perry, Y. Shao-Horn, Synthesis and activities of rutile IrO2 and RuO2 nanoparticles for oxygen evolution in acid and alkaline solutions, The journal of physical chemistry letters 3 (3) (2012) 399–404.
[16] T. Audichon, T.W. Napporn, C. Canaff, C.u. Morais, C.m. Comminges, K.B. Kokoh, IrO2 coated on RuO2 as efficient and stable electroactive nanocatalysts for electrochemical water splitting, J. Phys. Chem. C 120 (5) (2016) 2562–2573.
[17] D. Tan, H. Xiong, T. Zhang, X. Fan, J. Wang, F. Xu, Recent progress in noble-metal-free electrocatalysts for alkaline oxygen evolution reaction, Front. Chem. 10 (2022) 1071274.
[18] X. Chen, Z. Zhang, Y. Chen, R. Xu, C. Song, T. Yuan, W. Tang, X. Gao, N. Wang, L. Cui, Research advances in earth-abundant-element-based electrocatalysts for oxygen evolution reaction and oxygen reduction reaction, 2023.
[19] S. Wang, A. Lu, C.-J. Zhong, Hydrogen production from water electrolysis: role of catalysts, Nano Convergence 8 (1) (2021) 4.
[20] N. Han, W. Zhang, W. Guo, H. Pan, B. Jiang, L. Xing, H. Tian, G. Wang, X. Zhang, J. Fransaer, Designing oxide catalysts for oxygen electrocatalysis: insights from mechanism to application, Nano-Micro Letters 15 (1) (2023) 185.
[21] A. Raveendran, M. Chandran, R. Dhanusuraman, A comprehensive review on the electrochemical parameters and recent material development of electrochemical water splitting electrocatalysts, RSC Adv. 13 (6) (2023) 3843–3876.
[22] Y. Zhou, R. Lu, X. Tao, Z. Qiu, G. Chen, J. Yang, Y. Zhao, X. Feng, K. Müllen, Boosting oxygen electrocatalytic activity of Fe–N–C catalysts by phosphorus incorporation, J. Am. Chem. Soc. 145 (6) (2023) 3647–3655.
[23] A. Vazhayil, L. Vazhayal, J. Thomas, N. Thomas, A comprehensive review on the recent developments in transition metal-based electrocatalysts for oxygen evolution reaction, Appl Surf Sci Adv 6 (2021) 100184.
[24] X. Chen, J. Liu, T. Yuan, Z. Zhang, C. Song, S. Yang, X. Gao, N. Wang, L. Cui, Recent advances in earth-abundant first-row transition metal (Fe, co and Ni)-based electrocatalysts for the oxygen evolution reaction, Energy Materials 2 (4) (2022) 200028.
[25] M. Gong, H. Dai, A mini review of NiFe-based materials as highly active oxygen evolution reaction electrocatalysts, Nano Res 8 (2015) 23–39.
[26] A.K. Tareen, G.S. Priyanga, K. Khan, E. Pervaiz, T. Thomas, M. Yang, Nickel-based transition metal nitride electrocatalysts for the oxygen evolution reaction, ChemSusChem 12 (17) (2019) 3941–3954.
[27] Xiao-Hui Liu, Xiao-Long Jia, Ya-Ling Zhao, Rui-Xue Zheng, Qing-Lei Meng, Chang-Peng Liu, Wei Xing, Mei-Ling Xiao, Recent advances in nickel-based catalysts for electrochemical reduction of carbon dioxide, Advanced Sensor and Energy Materials. ISSN: 2773-045X 2 (3) (2023) 100073.
[28] M.N. Lakhan, A. Hanan, A.H. Shar, I. Ali, Y. Wang, M. Ahmed, U. Aftab, H. Sun, H. Arandiyan, Transition metals-based electrocatalysts for alkaline overall water splitting: advancements, challenges, and perspectives, Chem. Commun. 60 (2024) 5104–5135.
[29] H. Sheng, R.D. Ross, J. Schmidt, S. Jin, Metal-compound-based electrocatalysts for hydrogen peroxide electrosynthesis and the electro-Fenton process, ACS Energy Lett. 8 (1) (2022) 196–212.
[30] Y. Li, L. Hu, W. Zheng, X. Peng, M. Liu, P.K. Chu, L.Y.S. Lee, Ni/co-based nanosheet arrays for efficient oxygen evolution reaction, Nano Energy 52 (2018) 360–368.
[31] E. López-Fernández, C.G. Sacedón, J. Gil-Rostra, F. Yubero, A.R. González-Elipe, A. de Lucas-Consuegra, Recent advances in alkaline exchange membrane water electrolysis and electrode manufacturing, Molecules 26 (21) (2021) 6326.
[32] M. Hammad, S. Angel, A.K. Al-Kamal, A. Asghar, A.S. Amin, M.-A. Kräenbring, H. T. Wiedemann, V. Vinayakumar, M.Y. Ali, P. Fortugno, Synthesis of novel LaCoO3/graphene catalysts as highly efficient peroxymonosulfate activator for the degradation of organic pollutants, Chem. Eng. J. 454 (2023) 139900.
[33] P. Gerschel, S. Angel, M. Hammad, et al., Determining materials for energy conversion across scales: the alkaline oxygen evolution reaction, Carbon Energy 6 (2024) e608.
[34] O. Anwar, S. Bapat, J. Ahmed, X. Xie, J. Sun, D. Segets, Hansen parameter evaluation for the characterization of titania photocatalysts using particle size distributions and combinatorics, Nanoscale 14 (37) (2022) 13593–13607.
[35] S. Bapat, S.O. Kilian, H. Wiggers, D. Segets, Towards a framework for evaluating and reporting Hansen solubility parameters: applications to particle dispersions, Nanoscale advances 3 (15) (2021) 4400–4410.
[36] A.S. Amin, D. Lerche, A.S. Odungat, S.U. Boehm, T. Koch, F. Özcan, D. Segets, A procedure for rational probe liquids selection to determine Hansen solubility parameters, ChemCatChem 16 (6) (2024) e202301393.
[37] S. Süß, T. Sobisch, W. Peukert, D. Lerche, D. Segets, Determination of Hansen parameters for particles: a standardized routine based on analytical centrifugation, Adv. Powder Technol. 29 (7) (2018) 1550–1561.
[38] O. Anwar, A.S. Amin, A. Amin, M.A. Kräenbring, F. Özcan, D. Segets, Determination of Hansen parameters of nanoparticles: a comparison of two methods using Titania, carbon black, and silicon/carbon composite materials, Part. Part. Syst. Charact. 40 (11) (2023) 2300050.
[39] A. Jain, C. Marcks, L. Grebener, J. Johny, A.S. Odungat, M. Chatwani, M.-A. Kräenbring, A. Shaji, M.F. Tesch, A.K. Mechler, V. Vinayakumar, D. Segets, A proof-of-principle demonstration: exploring the effect of anode layer microstructure on the alkaline oxygen evolution reaction, Adv. Funct. Mater. 35 (2025) 2421352.
[40] M.-A. Kräenbring, F. Özcan, D. Segets, Analyzing emulsion dynamics via direct visualization and statistical methodologies, ACS Omega 9 (37) (2024) 39253–39258.
[41] S. Bapat, D. Segets, Sedimentation dynamics of colloidal formulations through direct visualization: implications for fuel cell catalyst inks, ACS Applied Nano Materials 3 (8) (2020) 7384–7391.
[42] N.P. Pham, J.N. Burghartz, P.M. Sarro, Spray coating of photoresist for pattern transfer on high topography surfaces, J. Micromech. Microeng. 15 (4) (2005) 691.
[43] F.-H. Wang, H.-P. Chang, C.-C. Tseng, C.-C. Huang, H.-W. Liu, Influence of hydrogen plasma treatment on Al-doped ZnO thin films for amorphous silicon thin film solar cells, Curr. Appl. Phys. 11 (1) (2011) S12–S16.
[44] T. Lim, S. Lee, M. Suh, S. Ju, Surface modification of oxide nanowires by nitrogen plasma, Electrochem. Solid-State Lett. 14 (5) (2011) H218.
[45] X. Kong, et al., Plasma-assisted synthesis of nickel-cobalt nitride–oxide hybrids for high-efficiency electrochemical hydrogen evolution, Materials Today Energy 21 (2021) 100784.
[46] J. Qi, W. Zhang, R. Cao, Porous materials as highly efficient electrocatalysts for the oxygen evolution reaction, ChemCatChem 10 (6) (2018) 1206–1220.
[47] S. Ghosh, H. Ohashi, H. Tabata, Y. Hashimasa, T. Yamaguchi, Microstructural pore analysis of the catalyst layer in a polymer electrolyte membrane fuel cell: a combination of resin pore-filling and FIB/SEM, Int. J. Hydrog. Energy 40 (45) (2015) 15663–15671.
[48] B. Ouyang, H. Qin, C. Sun, Y. Deng, A. Li, J. Zhu, E. Kan, R.S. Rawat, Tailored heterostructured Ni3N–NiO nano-frameworks for boosting electrocatalytic oxygen evolution via surface-modulated plasma strategy, Nano Res 17 (9) (2024) 7909–7917.
[49] Timo Wagner, Felix Schaumburg, Florian Kensy, Axel Lorke, Nicolas Wöhrl, Changes: optimizing morphology and chemistry of nickel surfaces by a scalable plasma process for hydrogen electrolyzers, Surf. Coat. Technol. ISSN: 0257-8972 505 (2025) 132056.
[50] A. Jain, V. Vinayakumar, A. Olean-Oliveira, C. Marcks, M. Chatwani, A.K. Mechler, C. Andronescu, D. Segets, From small-area observations to insight: surface-feature-extrapolation of anodes for alkaline oxygen evolution reaction, ChemCatChem 16 (5) (2024) e202301461.
[51] A.S. Odungat, L. Grebener, O. Pasdag, T.B. Nguyen, Y. Zhu, S. Kohsakowski, I. Radev, F. Özcan, D. Segets, A multiscale pore analysis method for polymer electrolyte membrane fuel cell catalyst layers validated and exemplified by correlating microstructure with production process parameters, Adv. Energy Sustainability Res. (2025) 2500043.
[52] B. Zhou, R. Gao, J.J. Zou, H. Yang, Surface design strategy of catalysts for water electrolysis, Small 18 (27) (2022) 2202336.
[53] B. Ouyang, Y. Zhang, Z. Zhang, H.J. Fan, R.S. Rawat, Nitrogen-plasma-activated hierarchical nickel nitride nanocorals for energy applications, Small 13 (34) (2017) 1604265.
[54] M. Shalom, D. Ressnig, X. Yang, G. Clavel, T.P. Fellinger, M. Antonietti, Nickel nitride as an efficient electrocatalyst for water splitting, J Mater Chem A 3 (15) (2015) 8171–8177.
[55] K. Kawashima, R.A. Márquez-Montes, H. Li, K. Shin, C.L. Cao, K.M. Vo, Y.J. Son, B. R. Wygant, A. Chunangad, D.H. Youn, Electrochemical behavior of a Ni 3 N OER precatalyst in Fe-purified alkaline media: the impact of self-oxidation and Fe incorporation, Materials Advances 2 (7) (2021) 2299–2309.
[56] M. Lyons, R. Doyle, I. Godwin, M. O'Brien, L. Russell, Hydrous nickel oxide: redox switching and the oxygen evolution reaction in aqueous alkaline solution, J. Electrochem. Soc. 159 (12) (2012) H932.
[57] M. Mattinen, J. Schröder, G. D'Acunto, M. Ritala, T.F. Jaramillo, M.B. Stevens, S. F. Bent, Dynamics of precatalyst conversion and iron incorporation in nickel-based alkaline oxygen evolution reaction catalysts, Cell Rep. Phys. Sci. 5 (11) (2024) 102284.
[58] F. Le Formal, L. Yerly, E. Potapova Mensi, X. Pereira Da Costa, F. Boudoire, N. Guijarro, M. Spodaryk, A. Züttel, K. Sivula, Influence of composition on performance in metallic iron–nickel–cobalt ternary anodes for alkaline water electrolysis, ACS Catal. 10 (20) (2020) 12139–12147.
[59] C.C. McCrory, S. Jung, J.C. Peters, T.F. Jaramillo, Benchmarking heterogeneous electrocatalysts for the oxygen evolution reaction, J. Am. Chem. Soc. 135 (45) (2013) 16977–16987.
[60] F. Dionigi, Z. Zeng, I. Sinev, T. Merzdorf, S. Deshpande, M.B. Lopez, S. Kunze, I. Zegkinoglou, H. Sarodnik, D. Fan, In-situ structure and catalytic mechanism of NiFe and CoFe layered double hydroxides during oxygen evolution, Nat. Commun. 11 (1) (2020) 2522.
[61] C. Gohlke, J. Gallenberger, N. Niederprüm, H. Ingendae, J. Kautz, J.P. Hofmann, A. K. Mechler, Boosting the oxygen evolution reaction performance of Ni-Fe-electrodes by tailored conditioning, ChemElectroChem 11 (18) (2024) e202400318.
[62] K. Xu, P. Chen, X. Li, Y. Tong, H. Ding, X. Wu, W. Chu, Z. Peng, C. Wu, Y. Xie, Metallic nickel nitride nanosheets realizing enhanced electrochemical water oxidation, J. Am. Chem. Soc. 137 (12) (2015) 4119–4125.
[63] J. Li, Z. Zhu, Y. Huang, F. Wang, Ni3N: a multifunctional material for energy storage and electrocatalysis, Mater. Today Energy 26 (2022) 101001.
[64] M. Yoshida, Y. Mitsutomi, T. Mineo, M. Nagasaka, H. Yuzawa, N. Kosugi, H. Kondoh, Direct observation of active nickel oxide cluster in nickel–borate electrocatalyst for water oxidation by in situ O K-edge X-ray absorption spectroscopy, J. Phys. Chem. C 119 (33) (2015) 19279–19286.

[65] M.F. Tesch, S.A. Bonke, R. Golnak, J. Xiao, A.N. Simonov, R. Schlögl, Vacuum compatible flow-cell for high-quality in situ and operando soft X-ray photon-in–photon-out spectroelectrochemical studies of energy materials, Electrochem. Sci. Adv. 2 (6) (2022) e2100141, https://doi.org/10.1002/elsa.202100141.
[66] A. Bergmann, T.E. Jones, E. Martinez Moreno, D. Teschner, P. Chernev, M. Gliech, T. Reier, H. Dau, P. Strasser, Unified structural motifs of the catalytically active state of co (oxyhydr) oxides during the electrochemical oxygen evolution reaction, Nat. Catal. 1 (9) (2018) 711–719.
[67] R.A. Krivina, Y. Ou, Q. Xu, L.P. Twight, T.N. Stovall, S.W. Boettcher, Oxygen electrocatalysis on mixed-metal oxides/oxyhydroxides: from fundamentals to membrane electrolyzer technology, Accounts of Materials Research 2 (7) (2021) 548–558.
[68] M.B. Stevens, L.J. Enman, E.H. Korkus, J. Zaffran, C.D. Trang, J. Asbury, M.G. Kast, M.C. Toroker, S.W. Boettcher, Ternary Ni-co-Fe oxyhydroxide oxygen evolution catalysts: intrinsic activity trends, electrical conductivity, and electronic band structure, Nano Res 12 (2019) 2288–2295.
[69] Y. Wu, Y. Li, Z. Xie, Y. Wang, Y. Wang, B. Wei, Tracking the structural evolution and activity origin of co-doped NiFe layered double hydroxide for enhanced oxygen evolution reaction, Chem. Eng. J. 488 (2024) 151086.
[70] D. Chen, X. Xiong, B. Zhao, M.A. Mahmoud, M.A. El-Sayed, M. Liu, Probing structural evolution and charge storage mechanism of NiO2Hx electrode materials using in operando resonance Raman spectroscopy, Adv. Sci. 3 (6) (2016).
[71] X. Yang, H. Zhang, B. Yu, Y. Liu, W. Xu, Z. Wu, An unveiled electrocatalysis essence of NiCo hydroxides through in situ Raman spectroscopy for urea oxidation, Energy Technol. 10 (5) (2022) 2101010.